



The commercial antibiotics with inherent AIE feature: In situ visualization of antibiotic metabolism and specifically differentiation of bacterial species and broad-spectrum therapy

Bingnan Wang^{a,b}, Lirong Wang^{a,b}, Haozhong Wu^{a,b}, Xiaolin Liu^d, Jiamiao Zhu^{a,b}, Rong Hu^{a,b}, Dan Ding^e, Anjun Qin^{a,b,*}, Ben Zhong Tang^{b,c,d,**}

^a State Key Laboratory of Luminescent Materials and Devices, Guangdong Provincial Key Laboratory of Luminescence from Molecular Aggregates, South China University of Technology, Guangzhou, 510640, China

^b Center for Aggregation-Induced Emission, AIE Institute, South China University of Technology, Guangzhou, 510640, China

^c School of Science and Engineering, Shenzhen Institute of Aggregate Science and Technology, The Chinese University of Hong Kong, Shenzhen, Guangdong, 518172, China

^d Hong Kong Branch of Chinese National Engineering Research Centre for Tissue Restoration and Reconstruction, The Hong Kong University of Science & Technology, Clear Water Bay, Kowloon, Hong Kong, China

^e State Key Laboratory of Medicinal Chemical Biology, Frontiers Science Center for Cell Responses, Key Laboratory of Bioactive Materials, Ministry of Education, College of Life Sciences, Nankai University, Tianjin, 300071, China

ARTICLE INFO

Keywords:

Aggregation-induced emission
Antibiotics
Antibacterial activity
In situ visualization

ABSTRACT

The research on pharmacology usually focuses on the structure-activity relationships of drugs, such as antibiotics, to enhance their activity, but often ignores their optical properties. However, investigating the photo-physical properties of drugs is of great significance because they could be used to *in situ* visualize their positions and help us to understand their working metabolism. In this work, we identified a class of commercialized antibiotics, such as levofloxacin, norfloxacin, and moxifloxacin (MXF) hydrochloride, featuring the unique aggregation-induced emission (AIE) characteristics. By taking advantage of their AIE feature, antibiotic metabolism in cells could be *in situ* visualized, which clearly shows that the luminescent aggregates accumulate in the lysosomes. Moreover, after a structure-activity relationship study, we found an ideal site of MXF to be modified with a triphenylphosphonium and an antibiotic derivative MXF-P was prepared, which is able to specifically differentiate bacterial species after only 10 min of treatment. Moreover, MXF-P shows highly effective broad-spectrum antibacterial activity, excellent therapeutic effects and biosafety for *S. aureus*-infected wound recovery. Thus, this work not only discovers the multifunctionalities of the antibiotics but also provides a feasible strategy to make the commercialized drugs more powerful.

1. Introduction

Every new disease, such as coronavirus disease 2019 (COVID-19), appears to be catastrophic to humans, and the emergence of targeted drugs can bring the hope of survival to dying patients; therefore, scientists have never been stopping exploring new drugs [1–3]. During drug development, researchers generally focus on their structure-activity relationships to continuously improve their activity

[4], while few studies have been put on their other functions, such as optical properties [5]. Most drugs, such as paclitaxel [6], artemisinin [7], and aspirin [8], lack a large conjugated system, resulting in a weak or ultraviolet emission, and making their observation by the naked eye difficult. However, the optical properties of drugs are an ideal way to understand their working mechanism [9]. Such investigation can determine the influences because of the structural differentiation on their optical properties and also monitor the changes in drug

Peer review under responsibility of KeAi Communications Co., Ltd.

* Corresponding author. State Key Laboratory of Luminescent Materials and Devices, Guangdong Provincial Key Laboratory of Luminescence from Molecular Aggregates, South China University of Technology, Guangzhou, 510640, China.

** Corresponding author. Center for Aggregation-Induced Emission, AIE Institute, South China University of Technology, Guangzhou, 510640, China.

E-mail addresses: msqinaj@scut.edu.cn (A. Qin), tangbenz@cuhk.edu.cn (B.Z. Tang).

<https://doi.org/10.1016/j.bioactmat.2022.11.002>

Received 20 September 2022; Received in revised form 23 October 2022; Accepted 8 November 2022

2452-199X/© 2022 The Authors. Publishing services by Elsevier B.V. on behalf of KeAi Communications Co. Ltd. This is an open access article under the CC BY-NC-ND license (<http://creativecommons.org/licenses/by-nc-nd/4.0/>).

concentration and position *in situ* to better understand metabolic processes, reduce toxicity and side effects, and achieve precision therapy. Therefore, the research on the optical properties of drugs is of great significance to visualize them *in situ* and effectively increase the understanding of their metabolism.

The fluorescence technology enjoying the advantages of simple operation, high sensitivity, and *in situ* process visualization has indeed applied in drug delivery and visualization [10–13]. However, the drugs have to be modified by attaching fluorophores [14], which often make the generate derivatives cannot accurately represent the drugs because their pharmaceutical activity and physicochemical properties are affected. In addition, there are often differences in drug endocytosis and/or phagocytosis between the pristine and modified drugs [15]. Therefore, the drugs themselves are highly emissive in the practically applicable states or their pharmaceutical activity does not affect after modification are the key for further study in this area.

Among the drugs, the antibiotics, such as the Food and Drug Administration (FDA)-approved fluoroquinolone antibiotics of norfloxacin (NOR), levofloxacin (LEV), and moxifloxacin hydrochloride (MXF-HCl) are widely used for the treatment of multiple infections because of their high efficiency, specificity, and biosafety. However, compared with the number of studies on their drug activity, the investigation on their optical properties is limited.

In this work, the optical properties of a series of commercial fluoroquinolone antibiotics were examined. We excitingly found that they possess the unique aggregation-induced emission (AIE) feature, a concept coined in our group in 2001 [16–36]. Through the density functional theory (DFT) calculation and single crystal structure investigation, we figured out the restriction of intramolecular motion (RIM) is the cause for the AIE feature [37]. By taking advantage of this feature, we were able to visualize these antibiotics *in situ* and observe their concentration changes in cells. Moreover, after a systematical structure-activity relationship study, we found an ideal site of MXF to be modified with a triphenylphosphonium without sacrifice of its pharmaceutical activity, and an antibiotic derivative MXF-P was prepared. Notably, MXF-P could specifically differentiate bacterial species after only 10 min of treatment. Therefore, this work not only identified and explained the AIE feature of fluoroquinolone antibiotics, but also found ideal sites for modification to realize multifunctional drugs, which provides an innovative strategy for new multifunctional drug discovery.

2. Materials and methods

2.1. Chemicals and biological samples

Norfloxacin and Levofloxacin were purchased from Energy Chemical. Moxifloxacin Hydrochloride was purchased from TCI. Ltd. PBS buffer, DMEM (Dulbecco's modified Eagle medium) and fetal bovine serum (FBS) were purchased from Thermo Fisher Scientific (Shanghai, China). MCF-7 cells and HeLa cells were obtained from cell culture center of Institute of Basic Medical Sciences, Chinese Academy of Medical Science (Beijing, China). *S. aureus* ATCC 6538 and *Candida albicans* (*C. albicans*) ATCC 10231 were obtained from China General Microbiological Culture Collection Center. The Amp Escherichia coli (*E. coli*) TOP 10 was purchased from Beijing Bio-Med Technology

Development Co.

2.2. Synthesis of EFODC and MXF-P

The synthetic route to EFODC is shown in Scheme 1. FODC (0.5 mmol, 103.5 mg) and K_2CO_3 (1.0 mmol, 138 mg) were placed into a 50 mL two-necked round bottom flask and then DMF (10 mL), ethyl bromide (2.0 mmol, 218 mg) were added under stirring. After the reaction was stirred for 12 h at 85 °C (the progress of the reaction was monitored by TLC), DMF was removed through vacuum evaporation to obtain intermediates. These intermediates were added to EtOH (6 mL) followed by addition of 2.0 M aq. NaOH solution (0.3 mL) dropwise. The reaction mixture was heated at 70 °C for 16 h. Subsequently, HCl (6 mL, 1 M) was added and the precipitate was filtered to afford a white solid EFODC in 72% yield. 1H NMR (400 MHz, $DMSO-d_6$) δ 15.01 (s, 1H), 9.08 (s, 1H), 8.17 (dd, $J = 9.6, 4.4$ Hz, 1H), 8.05 (dd, $J = 8.8, 3.2$ Hz, 1H), 7.90 (m, $J = 9.6, 8.0, 3.2$ Hz, 1H), 4.63 (q, $J = 7.2$ Hz, 2H), 1.42 (t, $J = 7.2$ Hz, 3H). ^{13}C NMR (125 MHz, $DMSO-d_6$) δ 177.4, 166.3, 161.0, 149.6, 136.4, 127.8, 123.3, 121.9, 110.9, 107.9, 49.8, 15.1. HRMS (MALDI-TOF) m/z $[M+Na]^+$ calcd for $C_{12}H_{10}FNO_3Na^+$ 258.0537, found 258.0536.

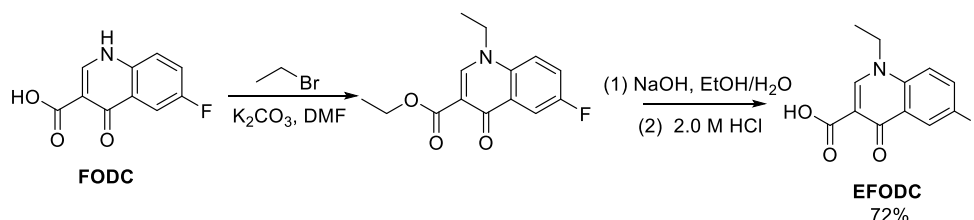
The synthetic route to MXF-P is shown in Scheme 2. Compound 1 (304 mg, 0.6 mmol) and antibiotic MXF-HCl (219 mg, 0.5 mmol) were dissolved in a mixed solution (10 mL, MeCN/DMF = 9:1). Afterward, $KHCO_3$ (84 mg, 1.0 mmol) was added. The reaction mixture was heated at 90 °C for 12 h. After the solvent was removed under reduced pressure, water was added, and the mixture was extracted with DCM (30 mL \times 3). The combined organic layer was dried with anhydrous Na_2SO_4 , concentrated and purified through silica gel column chromatography (eluent: DCM/MeOH = 20:1, v/v) to afford the yellow solid MXF-P in 58% yield. 1H NMR (500 MHz, $CDCl_3$) δ 15.16 (s, 1H), 8.37 (s, 1H), 7.84–7.75 (m, 9H), 7.71–7.65 (m, 7H), 4.02–3.99 (m, 1H), 3.80–3.71 (m, 3H), 3.65–3.55 (m, 5H), 3.17 (s, 1H), 2.76 (s, 1H), 2.53 (s, 1H), 2.39–2.23 (m, 3H), 1.82–1.41 (m, 10H), 1.37–1.17 (m, 5H), 0.99–0.92 (m, 2H). ^{13}C NMR (125 MHz, $CDCl_3$) δ 176.7, 167.2, 153.8, 149.5, 140.8, 135.0, 134.5, 133.8, 133.7, 133.6, 130.6, 130.5, 130.4, 118.8, 117.9, 107.71074, 61.4, 61.3, 55.4, 54.4, 49.1, 40.6, 37.0, 30.2, 29.7, 26.9, 23.8, 22.9, 22.6, 22.4, 14.1, 9.51. HRMS (MALDI-TOF) m/z $[M]^+$ calcd for $C_{45}H_{50}FN_3O_4P^+$ 746.3517, found 746.3509.

2.3. Cell imaging

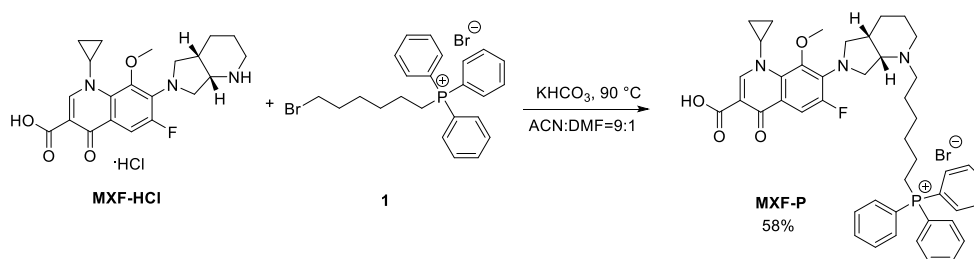
MCF-7 or HeLa cells were cultured overnight in a Petri dish with a coverslip. The cells were stained with 10 μ M LEV, MXF-HCl or MXF-P for different time followed by MitoTracker Red (100 nM) or LysoTracker Red (100 nM) for 30 min. The cells were observed by a laser scanning confocal microscope (LSM710, ZEISS) with a 5% laser power. Excitation filter: 405 nm for LEV, MXF-HCl or MXF-P, 543 nm for MitoTracker Red, 543 nm for LysoTracker Red; emission filter: 410–580 nm for LEV, 420–580 nm for MXF-HCl and MXF-P, 600–650 nm for MitoTracker Red, 600–650 nm for LysoTracker Red.

2.4. Bacteria imaging in cells

HeLa cells were cultured overnight in a Petri dish. Then, bacterial solution (20 μ L, $OD_{600} = 1.0$) was added into DMEM of HeLa cells. After



Scheme 1. Synthetic route to EFODC.



the mixture was incubated at 37 °C for 10 min, the blended solution was stained with 10 μM MXF-P. The infected cells were imaged by a laser scanning confocal microscope (LSM710, ZEISS) with 5% laser power. Excitation filter: 405 nm for MXF-P, emission filter: 420–600 nm for MXF-P.

2.5. Imaging of dead microorganisms

The *E. coli* and *C. albicans* were treated with 75% EtOH for 20 min

and then washed with PBS 3 times. Dead *E. coli* or *C. albicans* solution (100 μL , $\text{OD}_{600} = 1.0$) was added into 900 μL PBS solution with MXF-P (10 μM) and PI (3 $\mu\text{g}/\text{mL}$). Then, the mixture was incubated at 37 °C for 10 min the *E. coli* or *C. albicans* was harvested by centrifuging (7100 rpm for 2 min) and re-suspended in 15 μL of PBS. The stained mixture solution of 5 μL was added on glass slides, and then covered with a coverslip to fix bacteria. The samples were then imaged by confocal laser scanning microscopy.

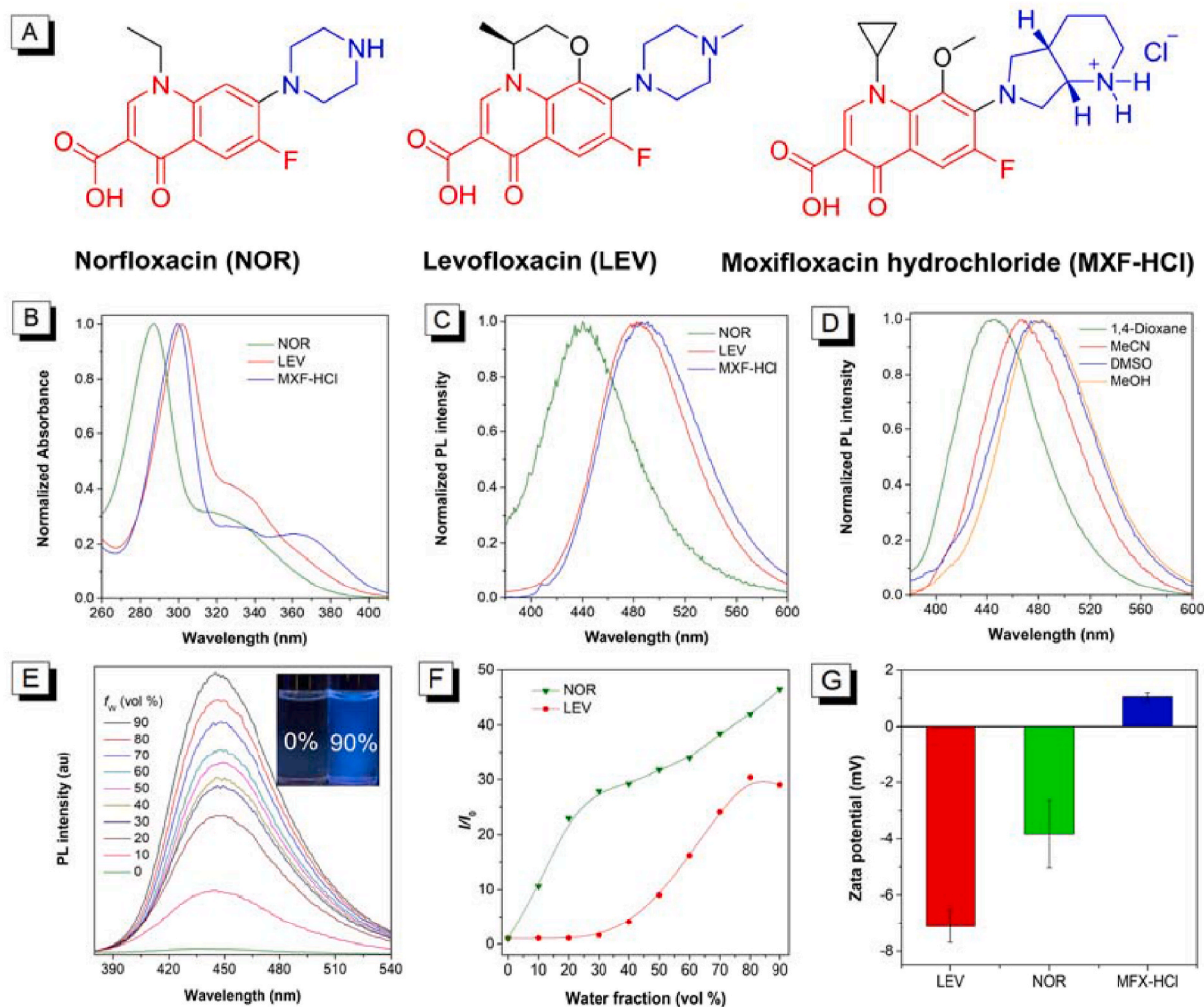


Fig. 1. (A) Chemical structures of the investigated fluoroquinolone antibiotics. (B) Normalized absorption spectra of NOR, LEV and MXF-HCl in DMSO solution. (C) Normalized photoluminescence (PL) spectra of the three antibiotics in DMSO solution. (D) Normalized PL spectra of LEV in different solvents. (E) PL spectra of NOR in DMSO mixtures with different volume fractions of water (f_w). Inset: Fluorescent photographs of NOR in DMSO with 0% and 90% water fraction. (F) Plots of I/I_0 versus the composition of the DMSO/water mixture, where I_0 is the lowest value of fluorescence intensity. (G) Zeta potentials of LEV, NOR, and MXF-HCl in aqueous solutions with 1% DMSO. The concentrations of antibiotics are all 10 μM in the photophysical property measurement. Excitation wavelength: 320 nm for NOR, 330 nm for LEV, 365 nm for MXF-HCl.

3. Results and discussion

3.1. Photophysical properties

The photophysical properties of the commercially available antibiotics of NOR, LEV and MXF-HCl were studied. Their structures and spectral information are shown in Fig. 1, and their photophysical data are summarized in Table S1. MXF-HCl showed a longer absorption peak at 362 nm than NOR (320 nm) and LEV (330 nm) in dilute DMSO solutions (Fig. 1B). Similarly, the emission peak of MXF-HCl (491 nm) is red-shifted compared with LEV (482 nm) and NOR (440 nm) in DMSO solutions (Fig. 1C and Table S1). Furthermore, a longer emission peak (473 nm) of MXF-HCl than those of NOR (396 nm) and LEV (457 nm) was clearly observed in the solid states (Fig. S1). These photophysical property could be ascribed to their donor- π -accepter structures by combining their distinct solvatochromism in the solvents of 1,4-dioxane, acetonitrile (MeCN), methanol (MeOH), and dimethyl sulfoxide (DMSO) with different polarity (Fig. 1D and S2). The red-shifted peaks of MXF-HCl is owing to its stronger electron-donating ability of the methoxyl group and (*S,S*)-2,8-diazabicyclo[4,3,0]noane moiety than the other antibiotics.

Next, we studied the photoluminescence (PL) properties of these antibiotics in different solvent mixtures (Fig. S3). As shown in Fig. 1E, since NOR has much better solubility in DMSO than in water, the PL intensity of NOR in DMSO solution strengthened with an increasing in water fraction (f_w) because of the formation of aggregates, unambiguously demonstrating that NOR is AIE active.

Similar AIE feature was observed for LEV (Fig. 1F and S3A). Because

MXF-HCl has good solubility in DMSO and water, the DMSO/water system is not suitable for characterizing its AIE properties, Therefore, we changed the solvent mixture to water/1,4-dioxane. When 1,4-dioxane was gradually added to its aqueous solution, the PL intensity of MXF-HCl was also progressively increased, exhibiting an aggregation-enhanced emission (AEE) characteristic. In addition, the absolute PL quantum yield (Φ_F) measurement showed that LEV, NOR, and MXF-HCl showed lower Φ_F values in DMSO solutions than in their solid states (Table S1), further confirming their AIE feature. Interestingly, the zeta potential experiments of the drug aggregates showed that LEV had a more negative potential value (-7.11 mV) than NOR (-3.84 mV), whereas MXF-HCl showed a positive value (1.4 mV) (Fig. 1G). This zeta potential reversal is owing to the protonation of MXF-HCl.

3.2. Mechanism of aggregation-induced emission

As shown in Fig. 1F, NOR displays the most distinct AIE feature. We thus took it as a model to investigate the underneath mechanism. For comparison, we purchased its intermediate FODC and synthesized EFODC (Scheme 1 and Fig. 2A, and S4-S6, the experimental details are provided in the Supporting Information). The photophysical property study showed that the absorption spectra of FODC and EFODC are quite similar in their DMSO solutions, and FODC and EFODC showed longer emission in the solid states than that in DMSO solutions (Fig. S7 and Table S2). Next, the emission behaviors of FODC and EFODC were studied in DMSO/water mixtures. The PL intensity of FODC decreased when large amounts of water was added into its DMSO solution (Fig. 2B), and its Φ_F in DMSO solution (4.9%) is higher than that in solid

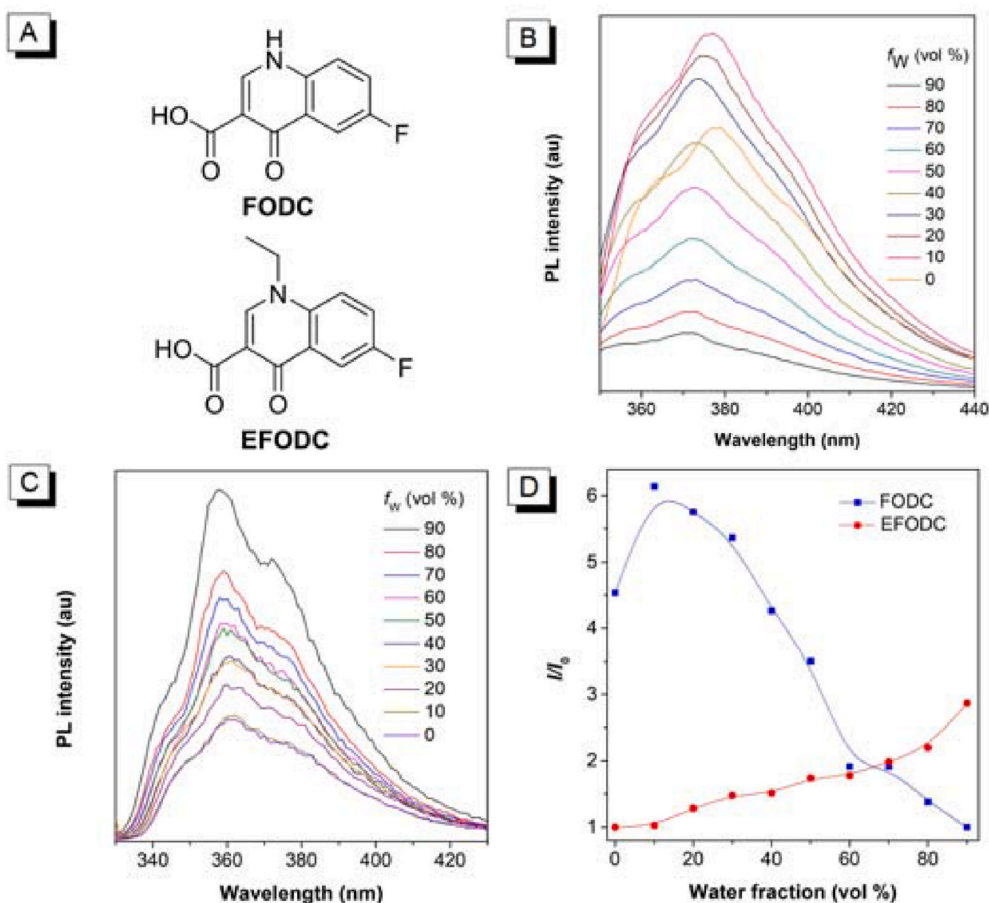


Fig. 2. (A) Molecular structures of FODC and EFODC. (B) PL spectra of FODC and (C) EFODC in DMSO mixtures with different volume fractions of water (f_w). Concentration: 10 μ M. Excitation wavelength: 330 nm. (D) Plots of I/I_0 values versus the composition of the DMSO/water mixture where I_0 is the lowest value of fluorescence intensity.

state (2.5%), displaying a typical aggregation-caused quenching (ACQ) effect. Whereas EFODC shows an AIE effect under the same conditions (Fig. 2C) and it gives a lower Φ_F (0.8%) in DMSO solution than in the solid state (2.1%). This low Φ_F of EFODC in DMSO solution might be related to the ethyl groups, the active motion from which might dissipate the excited state energy, while this motion was greatly restricted in the solid state, resulting in an increased Φ_F . Notably, when the f_w increased from 0% to 90%, NOR also exhibits more obvious AIE effect than EFODC (Figs. 2D and 1F). From these data and according to the structural characteristics of these antibiotics, we proposed that their AIE effect was caused by RIM.

3.3. Theoretical calculation

To better understand the discrepancies in the AIE properties of LEV, NOR, and MXF-HCl, we tried to employ DFT calculations to study these antibiotics. The calculation result could not be obtained for MXF-HCl due to the convergence failure during the optimization process. Therefore, the theoretical calculation for NOR and LEV are performed and the results are presented in Fig. 3. The optimal geometries of them show that the angles between the donor piperazine ring and the acceptor fluoroquinolone ($\theta = 12.5^\circ$ for NOR, and 30.5° for LEV) are small in the ground state. While, in the excited state, the larger θ values (78.1° for NOR, and 80.1° for LEV) suggest that they show a twisted intramolecular charge transfer (TICT) process. In addition, the molecular orbital distribution results show that in the ground state, holes of NOR and LEV are mostly distributed around whole molecule, and electrons are essentially localized on the fluoroquinolone moiety. Whereas, in the excited state, the holes are mainly distributed around the piperazine rings, and the electrons were localized on the fluoroquinolone moieties, which resulted in a negligible oscillator strength ($f = 0.000$). The separated distributions of the holes and electrons suggested that they showed distinct charge separation. Thus, in the solution states, the TICT process of the molecule might quench their emissions, and the motions of the donor piperazine were limited in the aggregate state, recovering

the bright fluorescence.

To further understand the luminescent behavior of the antibiotics in the aggregate state, we retrieved the single crystal structures of NOR, LEV, and MXF-HCl from the literature [38–40]. As shown in Fig. 4, the intermolecular C–H \cdots O, C–H \cdots C, and C–H \cdots F interaction distances in NOR are in the range of 1.992–2.891 Å, well rigidifying its conformation at the molecular level and limiting the motion of both the piperazine rings and ethyl groups. In addition, the intermolecular center distance between O₁ and O₂ of the benzene ring is 4.324 Å, and the vertical distance from O₁ to the plane of the quinoline ring is 3.517 Å, which is not conducive to forming the intermolecular π – π interactions that commonly quench emission. Therefore, the weak emission of NOR in DMSO solution might be that the active motion of the piperazine ring and ethyl group dissipates the excited state energy. However, in the solid or aggregate state, nonradiative decay was greatly inhibited, resulting in increased PL intensity.

Similarly, we found that these intermolecular C–H \cdots O, C–H \cdots C interactions are also present in LEV and MXF-HCl and that the distance between the adjacent benzene ring centers (3.990 Å for LEV and 4.460 Å or 3.829 Å for MXF-HCl) is further far compared with that of NOR. In addition, because of the introduction of the lateral resistance ethyl and cyclopropyl groups to the fluoroquinolone moiety, the intramolecular π – π interaction was disrupted (Fig. S8). These data well explain why these antibiotic molecules display enhanced PL in their solid or aggregate states.

3.4. pH-dependent fluorescence response of LEV

When a drug is administered, pH value should be studied because it will affect its solubility, absorption, metabolism, and pharmaceutical effects. To investigate how pH differences affect drug luminescence, we selected LEV, with a long emission wavelength and no protonation, as the model antibiotic. As shown in Fig. S9, under an ultraviolet light irradiation, LEV in PBS solution displayed green fluorescence with a pH value lower than 6.0 and blue fluorescence when the pH value increases

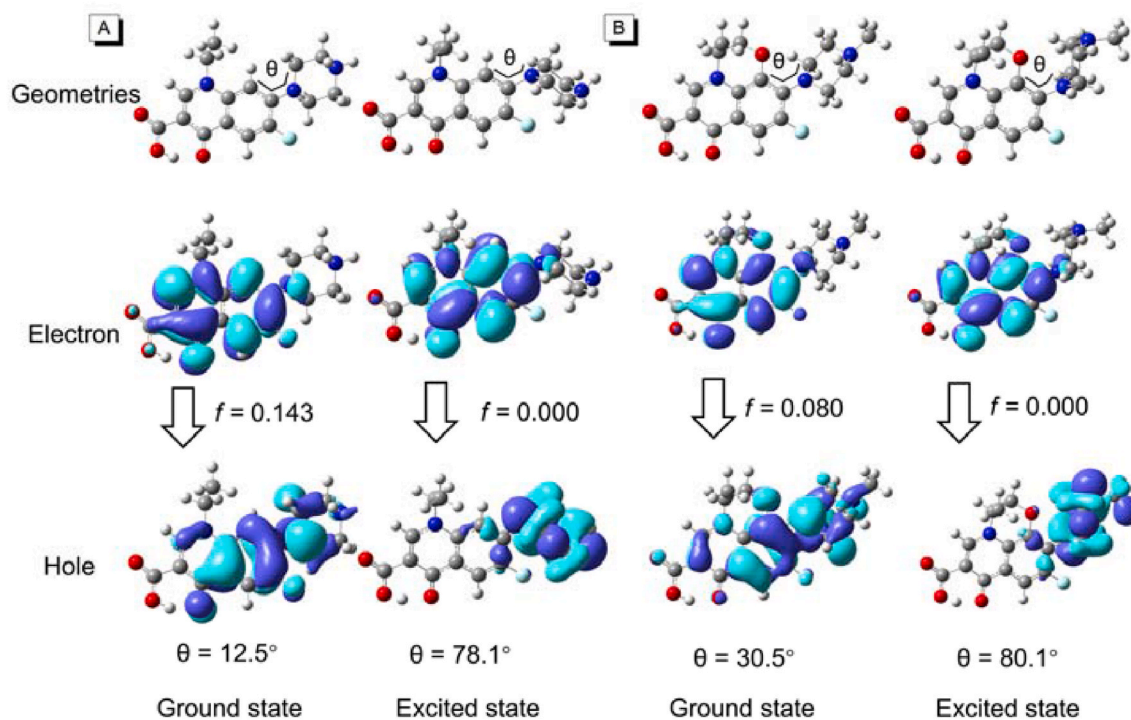


Fig. 3. The molecular geometries and the distributions of electron and hole natural transition orbitals (NTOs) for (A) NOR and (B) LEV in their optimized ground states and excited states calculated at the B3LYP/6-31g** level. θ and f are the angle between the piperazine ring and the fluoroquinolone and the oscillator strength, respectively.

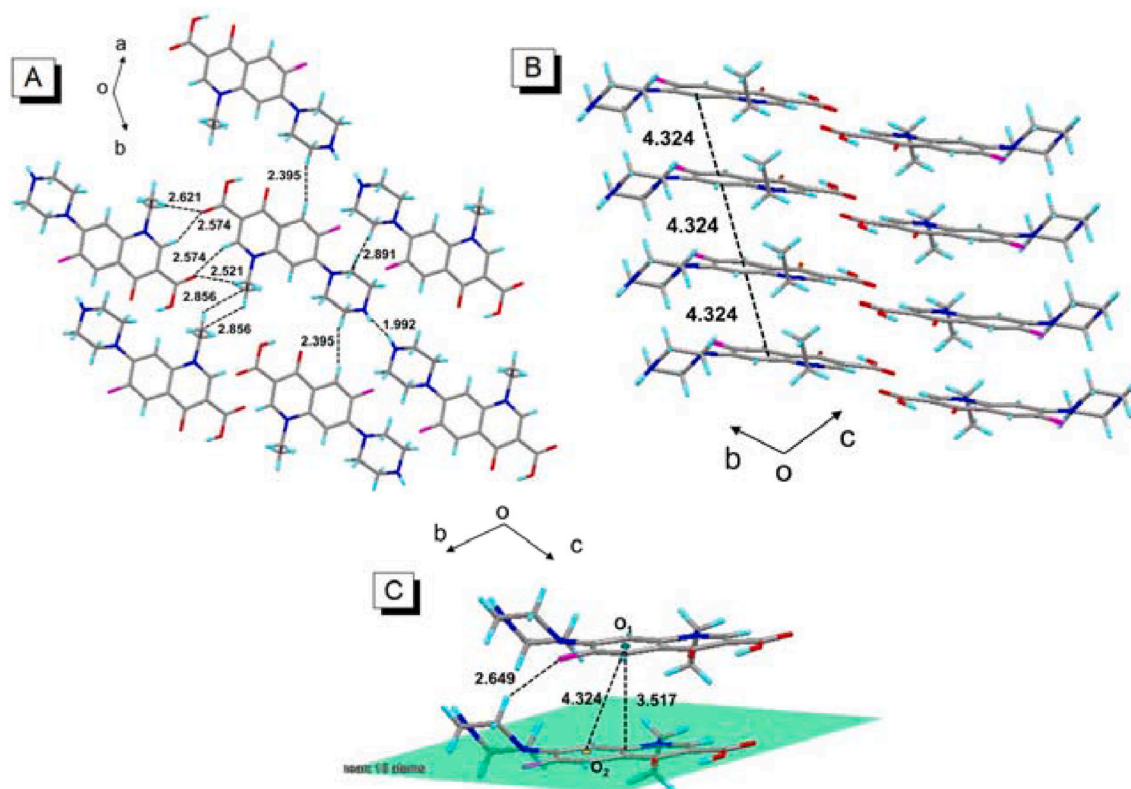


Fig. 4. Single crystal stacking diagram of NOR. (A) Intermolecular interactions. (B) The central distance of adjacent molecules. (C) The central and vertical distances of adjacent molecules.

to 7.0. Next, the absorption and PL spectra of LEV with different pH values were systematically investigated (Figs. S9B and S9C). The absorption spectra of LEV showed slight changes when the pH values increased from 1 to 13, however, its PL intensity and the maximum emission peaks changed drastically. From pH 1 to 5, the PL intensity gradually increased, and the emission peaks are at approximately 500 nm, whereas from pH 7 to 13, the PL intensity declined constantly, and the emission peaks exhibited an obvious blue-shift to about 460 nm (Figs. S9C and S9D). The fluctuation in PL intensity is because of the aggregate formation. In the strongly acidic or basic environments, the positively and negatively charged ionic LEV molecules that are formed through ionization have good solubility, leading to a weak PL intensity. Under neutral conditions, LEV formed aggregates because of its poor solubility in PBS solution, resulting in enhanced fluorescence.

To understand the pH-dependent PL response of LEV, we further studied the structural influences at different pH values by ^1H NMR spectroscopy (Fig. S10). After addition of trifluoroacetic acid (TFA), both the position and peak profile of the protons on the piperazine ring changed significantly, and a new peak appeared at δ 9.82 (Fig. S11), suggesting that the nitrogen atom of the piperazine ring was protonated. In addition, the carboxylic acids in LEV readily converted to carboxylic anions under basic conditions. Thus, the PL variation of LEV was caused by the changes in the molecular structure under different pH conditions.

3.5. In situ visualization of the drugs in cells

In situ visualization of drugs is important to understand their concentration, distribution, and metabolism in cells, and will help to reduce side effects and achieve precision therapy. Thanks to the AIE effect of LEV, NOR and MXF-HCl, we chose LEV and MXF-HCl as representative antibiotics to study the visualization process in cells because they possess longer emission wavelengths and higher Φ_F values. First, to study the change of antibiotic concentration over time in cells, we added

LEV to MCF-7 cells for cultivation. After 10 h, fluorescent images were acquired by confocal laser scanning microscopy (CLSM), but no signal was observed. Extension the incubation time to 24 h leads to a weak fluorescent signal near the nuclei of the MCF-7 cells, which was continuously enhanced with further elongation of time. This phenomenon was probably due to the slow entry and accumulation of LEV into the cells (Fig. 5A and B). Notably, thanks to its better water solubility, the fluorescent signal of MXF-HCl could be observed in cells after 24 h, which is faster than that of LEV. To determine the intracellular locations of LEV and MXF-HCl, colocalization experiments were performed with LysoTracker Red (LTR), a commercial lysosomal dye. The signals from LEV and MXF-HCl overlapped well with that of the LTR (Fig. 5C and D). Thus, these results revealed that LEV and MXF-HCl accumulated in lysosomes after entering the cells.

3.6. Modifying antibiotics for rapid identification and bacteria killing

To improve the pharmacological activities and develop novel functions of antibiotics, modification becomes an attractive strategy. Herein, we further investigated the antibacterial activities of NOR and its precursors of FODC and EFODC against *Staphylococcus aureus* (*S. aureus*) and *Escherichia coli* (*E. coli*) to acquire their structure-activity relationship and the right modification site. As shown in Fig. 6, compared with NOR, FODC and EFODC displayed notably decreased antibacterial activity against *S. aureus* and *E. coli*, suggesting that the introduction of the piperazine ring significantly improves the antibacterial activity. Moreover, EFODC and NOR showed stronger killing activity against *E. coli* than against *S. aureus*, while FODC did not exhibit antibacterial effect. These results suggest that the introduction of an ethyl group and piperazine ring on the fluoroquinolone ring could readily enhance the antibacterial activity.

According to a structure-activity relationship study on antibiotics [41,42], and above antibacterial activities of FODC, EFODC, and NOR, it

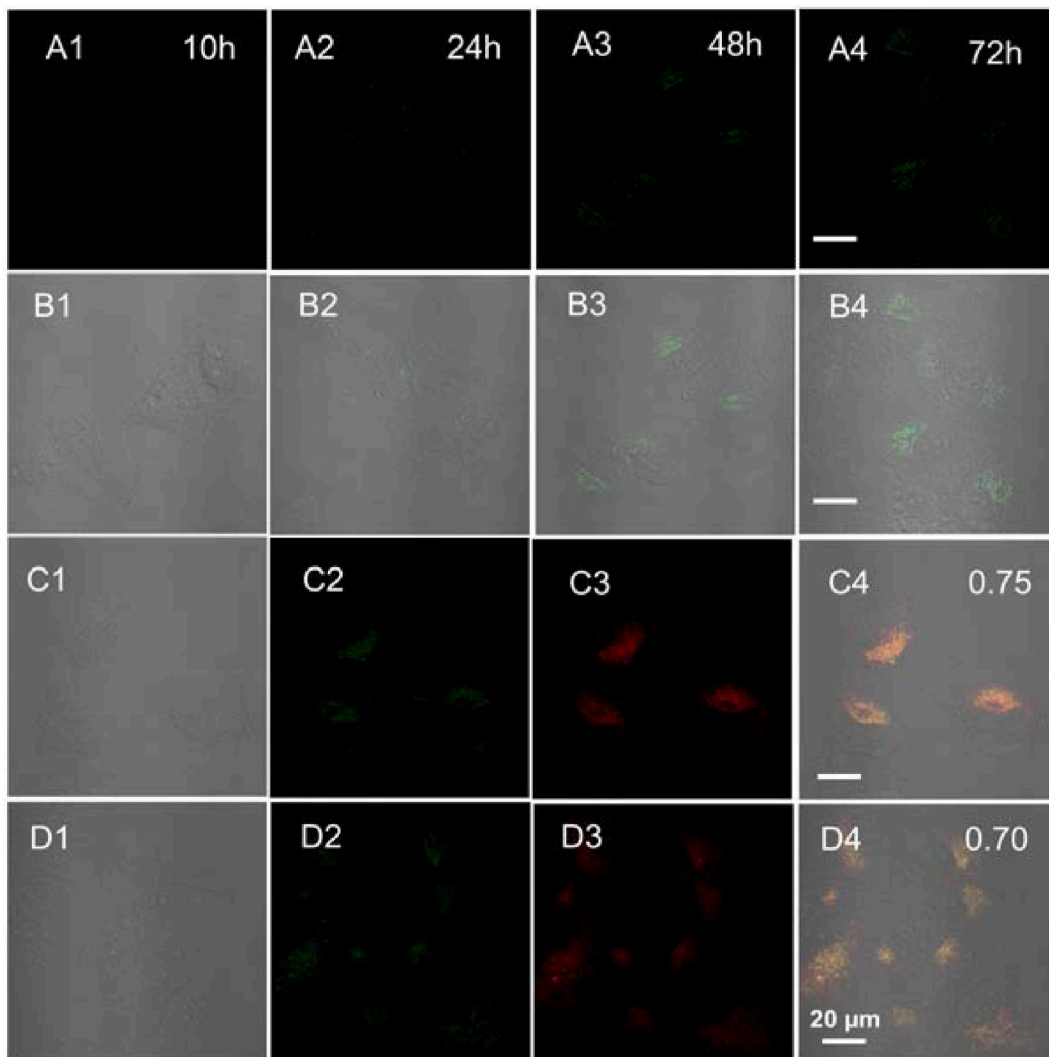


Fig. 5. (A–B) In situ visualization of LEV after incubation for different time by fluorescence imaging. (A1–A4) Fluorescent images of MCF-7 cells incubated with LEV for different time. (B1–B4) Bright field images. (C–D) Colocalization imaging of MCF-7 cells incubated with LysoTracker Red and antibiotics. (C1, D1) Bright field images. Fluorescent images of MCF-7 cells incubated with (C2) LEV for 72 h, (D2) MXF-HCl for 24 h, and (C3, D3) LysoTracker Red for 30 min (C4, D4) Merged images and the pearson’s correlation coefficients were 0.75 and 0.70, respectively. Concentration: 10 μM for LEV and MXF-HCl, 100 nM for LysoTracker Red. Scale bar: 20 μm .

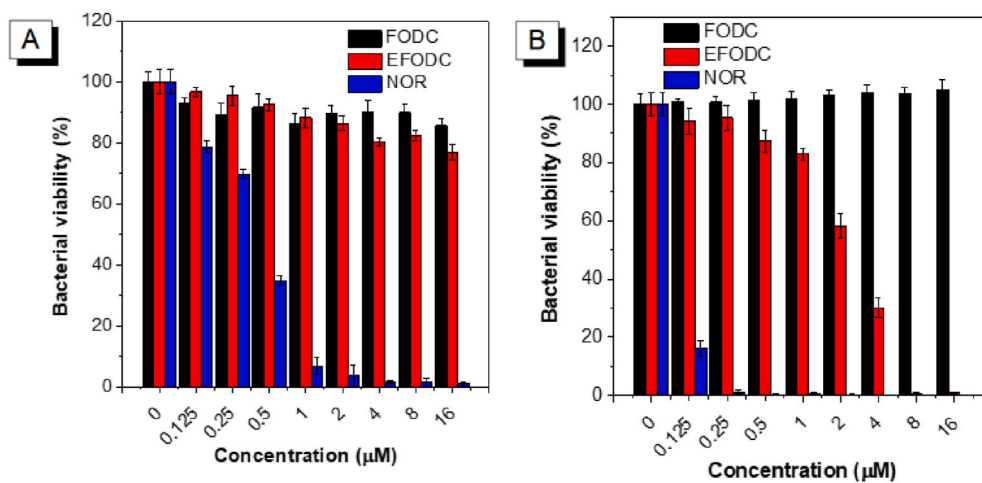


Fig. 6. Antibacterial tests of FODC, EFODC and NOR against *S. aureus* (A) and *E. coli* (B).

was suggested that the modification of secondary amine of MXF-HCl could maintain the antibacterial activity, but the derivation from carboxylic acid greatly affects its activity. In addition, the introduction of positively charged ionic groups would further enhance the solubility of the antibiotic and promote interaction with microorganisms with a negative membrane potential via electrostatic interactions [43,44]. Therefore, we covalently attached a triphenylphosphonium to MXF and generated a new multifunctional antibiotic of MXF-P (Scheme 2 and Fig. 7A).

After confirming the molecular structure of MXF-P (Fig. 7A and S12–S14), its photophysical properties were investigated. The MXF-P gave absorption and PL peaks at 364 nm and 470 nm in DMSO solution, respectively. Moreover, the emission was slightly red-shifted in the solid state (481 nm) (Fig. S15) and its Φ_F value in the solid state (7.4%) is higher than that in DMSO solution (1.3%), demonstrating that MXF-P is also AIE-active. The AIE feature of MXF-P was also confirmed by the enhanced PL intensity upon adding water into its DMSO solution (Fig. S16 and Table S3). Similar with MXF-HCl, MXF-P showed obvious solvatochromic effect because of its donor- π -acceptor structure. These results confirmed that the modified antibiotic retained the AIE feature.

To determine whether MXF-P have the same intracellular distribution as MXF-HCl, its colocalization experiment with LTR was conducted. The results indicated that the signals from MXF-P and LTR overlapped poorly (Fig. S17). Instead, MXF-P showed a quite similar regional distribution with MitoTracker Red (MTR), a commercial mitochondrial

dye. This was ascribed to the electrostatic interaction between the positively charged MXF-P and the negatively charged mitochondria [45, 46].

Thanks to its unique structure and AIE feature that enable a rapid identification of species and long-term bacterial tracking [47–56], MXF-P was chosen to distinguish the types of microorganisms. Generally, traditional Gram-staining method is difficult to track and monitor live bacteria over a long period of time, and the Gram-staining process is quite complicated, requiring multiple washes and a variety of reagents. As shown in Fig. 7B, MXF-P and MXF-HCl were used for the staining of *S. aureus*, and MXF-P showed a uniform *S. aureus* staining even after as short as 10 min while MXF-HCl did not. This is because the triphenylphosphonium group of MXF-P exhibits a stronger binding affinity than MXF-HCl toward the negatively charged *S. aureus*. Next, the negatively charged bacteria *E. coli* and the fungus *Candida albicans* (*C. albicans*) were incubated with MXF-P under the same experimental conditions, but no signals were observed. To verify the ability to distinguish different species in complex mixtures of microorganisms, these three species were mixed, and a staining experiment was carried out. It was found that MXF-P could rapidly and specifically identify and stain *S. aureus* (Fig. 7B), which showed excellent specific staining behavior among the reported cationic AIE luminogens (Table S4).

This phenomenon of specific staining was also speculated to be related to the outer membrane structures and permeability of the microorganisms. To verify this hypothesis, *E. coli* and *C. albicans* were

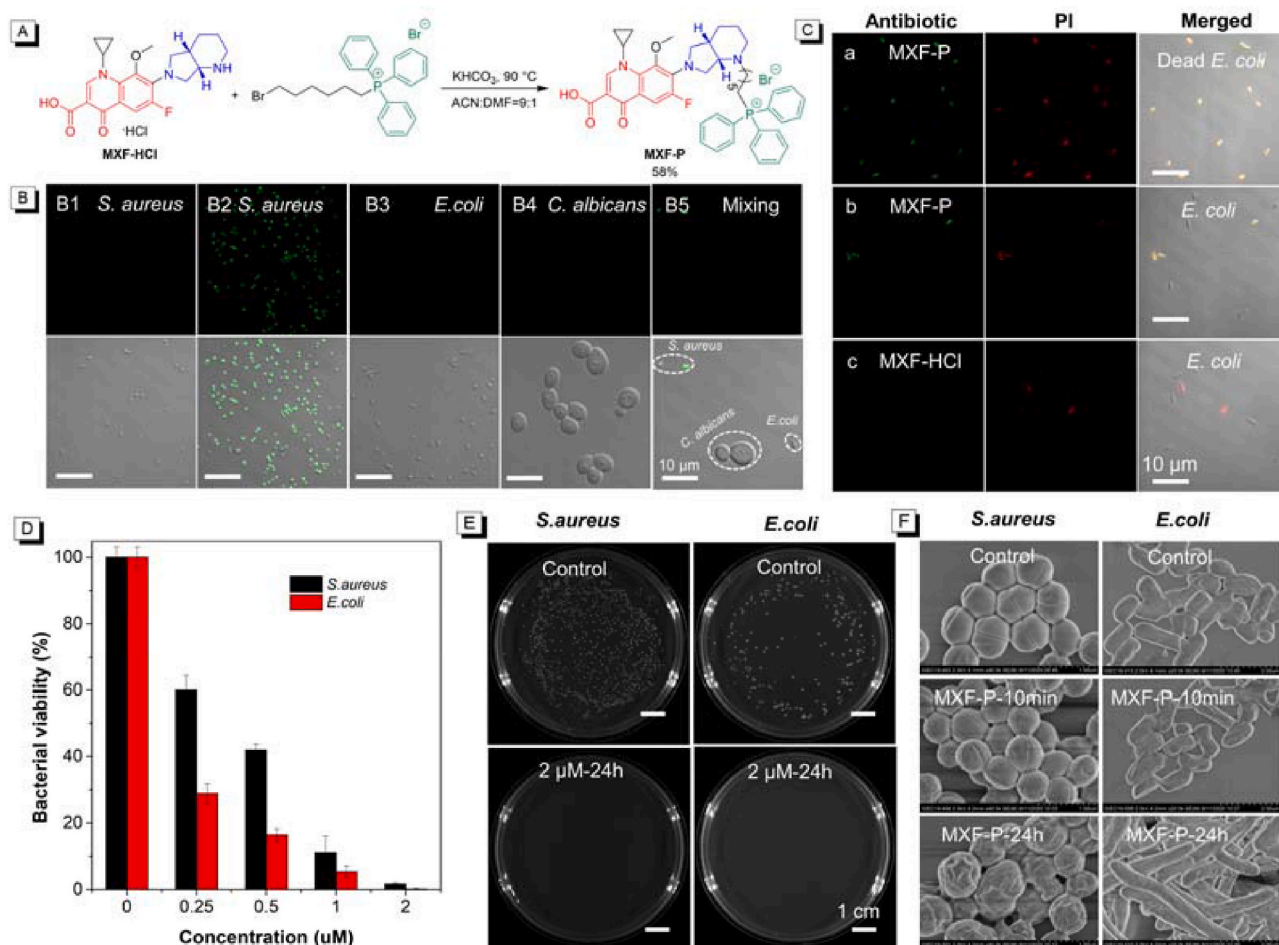


Fig. 7. (A) Synthetic route to MXF-P. (B) CLSM images of (B1) MXF-HCl and (B2–B5) MXF-P for the different microorganism strains. The mixed microorganisms included *S. aureus*, *E. coli*, and *C. albicans*. Scale bar: 10 μm. (C) Fluorescence and merged images of a) ethanol-treated *E. coli*, b) normal *E. coli* incubated with MXF-P and PI, and c) normal *E. coli* incubated with MXF-HCl and PI for 10 min. Scale bar: 10 μm. (D) Antibacterial activity against *S. aureus* and *E. coli* in nutrient broth culture with different concentrations of MXF-P. E) Antibacterial effect comparison diagram between the control group and 2 μM MXF-P treatment for 24 h. F) Morphological changes in bacteria treated with 10 μM MXF-P for different time using SEM.

killed by treatment with 75% ethanol for 20 min. The following staining results showed that the dead *E. coli* and *C. albicans* could be thoroughly stained with MXF-P because the membranes of dead microorganisms are more permeable than those of living ones (Fig. 7C and S18). It is worth noting that MXF-HCl could not identify dead microorganisms, demonstrating the powerfulness and advantage of MXF-P over MXF-HCl. In addition, thanks to the rapid staining ability of gram-positive bacteria, MXF-P was applied to quickly identify the bacteria in *S. aureus*-infected cells. The results of real-time and *in situ* fluorescence imaging showed that the positively charged MXF-P could quickly interact with *S. aureus* to show a signal and rapidly visualize the bacteria in cells (Fig. S19).

3.7. Antimicrobial activity of MXF-P

After proving that MXF-P possesses better luminescence and staining effect toward microorganisms than its parent antibiotic of MXF-HCl, we investigate its pharmacological activity and cytotoxicity because modified drugs generally will lose their pharmacological activity and may cause cytotoxicity problems. The cytotoxicity of MXF-P in NIH3T3 and HeLa cells was tested with a standard MTT assay. The viabilities of these cells were over 90% after treatment with 16 μM MXF-P (Fig. S20), thereby revealing its excellent biocompatibility. Then, we determined the minimum inhibitory concentrations (MICs) of MXF-P against *S. aureus* and *E. coli*. The MIC values of MXF-P for these two bacteria were approximately 1 μM , which is lower than that of related AIE luminogens and higher than that of known antibiotics (Table S5), and the antibacterial activity of MXF-P against *E. coli* was distinctly superior over that against *S. aureus* (Fig. 7D). Moreover, the bacteria lost their reproductive capacity after they were incubated with 2 μM MXF-P for 24 h, suggesting that MXF-P retained admirable antibacterial activity (Fig. 7E).

To better explore the antibacterial mechanism of MXF-P towards bacteria, the morphology of the treated bacteria was characterized using

scanning electron microscopy (SEM). As shown in Fig. 7F, when *S. aureus* and *E. coli* were treated with MXF-P for 10 min, their membrane surface and sizes did not change significantly, whereas when the treatment was elongated to 24 h, notably different effects were observed. The membrane structure of *S. aureus* became folded and contracted, which might be caused by the binding of the triphenyl phosphine salt of MXF-P to its membrane. Whereas, the membrane structure of *E. coli* remained intact but its size increased, which was attributed to the pharmaceutical activity of bacterial division inhibition [57].

In addition, MXF-P could produce reactive oxygen species (ROS) in bacteria (Fig. S21), which will further promote the antibacterial process [58]. We therefore could conclude that the antibacterial activity of MXF-P originated from the inhibition of bacterial division and destruction of the membrane structure.

3.8. *In vivo* antimicrobial activity of MXF-P

After confirming the superior antibacterial activity of MXF-P, we applied it to treat *S. aureus*-infected wounds in mice. As shown in Fig. 8, after PBS, MXF-HCl, or MXF-P sprayed on the infected wound areas of the mice and observed for 11 days, it was found that MXF-HCl and MXF-P showed similar wound recovery effects, which were superior over that of the PBS control group (Fig. 8A and B and S22). Notably, the weights of mice in the treatment groups increased faster than that in the PBS control group (Fig. 8C). Moreover, to further investigate the biosafety of MXF-P, the levels of the liver biomarkers ALT, AST, ALP and ALB and the kidney biomarkers CREA and BUN were tested from blood samples (Fig. 8D and E). The results suggested that no significant differences between treatments was found and they remain at normal levels [59]. In addition, the hematoxylin and eosin (H&E) staining experiments of organs of heart, kidney, liver, lung and spleen suggested that no organ damage or inflammatory lesions was observed (Fig. S23). These results

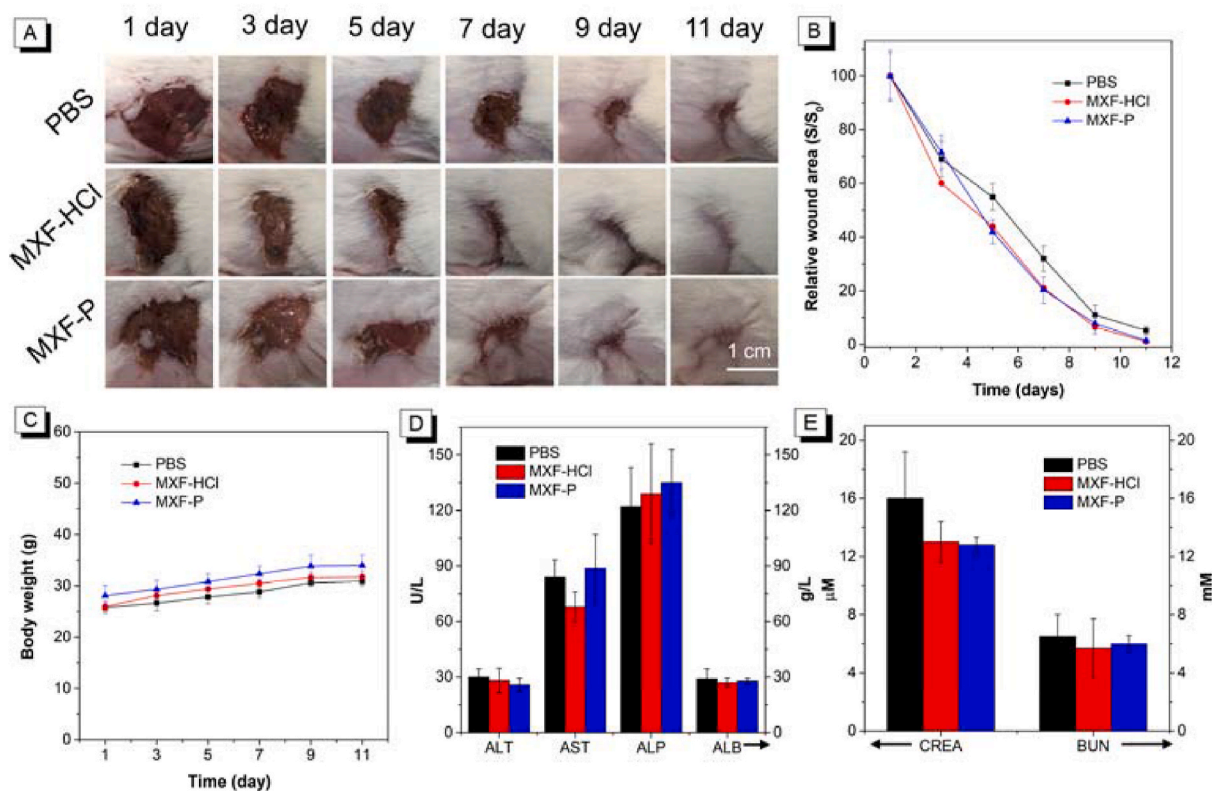


Fig. 8. (A) Photographs of the *S. aureus*-infected mouse wounds after different treatments. Scale bar: 1 cm. (B) The changes in the relative wound areas and (C) body weights of the mice over time. (D) Levels of ALT, AST, ALP and ALB and (E) CREA and BUN in blood samples taken from mice after different treatments.

well revealed that MXF-P could be used as a therapeutic reagent to treat clinical bacterial infections.

4. Conclusion

The commercially available fluoroquinolone antibiotics NOR, LEV, and MXF-HCl were found to be AIE active. By comparing the photo-physical properties and single crystal structures of NOR and its derivatives, we confirmed that their AIE feature was caused by the RIM. Thanks to their AIE feature, the drugs could be used to visualize their position in cells and the results show that they were accumulated in the lysosomes of cells. It is worth noting that the modified antibiotic of MXF-P could specifically stain gram-positive bacteria and distinguish between dead and live gram-negative bacteria via fluorescence imaging. In addition, MXF-P possesses effective broad-spectrum antibacterial activity as a result of its ability to inhibit bacterial division and cause outer membrane damage, showing excellent therapeutic effects and biosafety during *S. aureus*-infected wound recovery in mice. This work not only discovers the AIE feature to fluorescently visualize the positions in cells of fluoroquinolone antibiotics besides the well-known pharmaceutical activity but also provides a promising strategy to furnish the drugs with addition functions.

Ethics statements

Animal experiment protocols were reviewed and approved by South China Agricultural University and complied with all relevant ethical regulations.

Declaration of competing interest

All authors declare that they have no conflict of interest.

Ethics approval and consent to participate

Animal experiment protocols were reviewed and approved by South China Agricultural University and complied with all relevant ethical regulations. (Approval number: 2021c075).

CRedit authorship contribution statement

Bingnan Wang: conceived the experiments, was responsible for synthesizing compounds, spectral testing, analysis, and biological experiments, were responsible for antimicrobial experiments in vivo, contributed to the writing of this paper. **Lirong Wang:** were responsible for antimicrobial experiments in vivo, contributed to the writing of this paper. **Haozhong Wu:** was responsible for theoretical calculations, provided the suggestions in the experimental process, contributed to the writing of this paper. **Xiaolin Liu:** provided the suggestions in the experimental process, and contributed to the writing of this paper. **Jiamiao Zhu:** were responsible for antimicrobial experiments in vivo, provided the suggestions in the experimental process, contributed to the writing of this paper. **Rong Hu:** provided the suggestions in the experimental process, contributed to the writing of this paper. **Dan Ding:** provided the suggestions in the experimental process, contributed to the writing of this paper. **Anjun Qin:** conceived the experiments, provided the suggestions in the experimental process, contributed to the writing of this paper. **Ben Zhong Tang:** conceived the experiments, provided the suggestions in the experimental process, contributed to the writing of this paper.

Declaration of competing interest

All authors declare that they have no conflict of interest.

Acknowledgments

This work was financially supported by the National Natural Science Foundation of China (21788102, 21525417, and 51620105009), the Natural Science Foundation of Guangdong Province (2019B030301003, and 2016A030312002), the National Key Research and Development Program of China (Intergovernmental cooperation project, 2017YFE0132200) and the Innovation and Technology Commission of Hong Kong (ITC–CNERC14S01). We thank Prof. Peng Qian and Mr. Pang Yu for their support and help during the experiment.

Appendix A. Supplementary data

Supplementary data to this article can be found online at <https://doi.org/10.1016/j.bioactmat.2022.11.002>.

References

- [1] B. Yu, J. Chang, Azvudine (FNC): a promising clinical candidate for COVID-19 treatment, *Signal Transduct. Targeted Ther.* 5 (1) (2020) 236.
- [2] Z. Ren, H. Luo, Z. Yu, J. Song, L. Liang, L. Wang, H. Wang, G. Cui, Y. Liu, J. Wang, Q. Li, Z. Zeng, S. Yang, G. Pei, Y. Zhu, W. Song, W. Yu, C. Song, L. Dong, C. Hu, J. Du, J. Chang, A randomized, open-label, controlled clinical trial of azvudine tablets in the treatment of mild and common COVID-19, a pilot study, *Adv. Sci.* 7 (19) (2020), 2001435.
- [3] J. Wang, Fast identification of possible drug treatment of coronavirus disease-19 (COVID-19) through computational drug repurposing study, *J. Chem. Inf. Model.* 60 (6) (2020) 3277–3286.
- [4] K. Devendra, S. Sahil, K. Sourav, S. Gurpreet, M. Vikramdeep, K. Bhupinder, Medicinal perspective of indole derivatives: recent developments and structure-activity relationship studies, *Curr. Drug Targets* 21 (9) (2020) 864–891.
- [5] Y. Zhao, R.T.K. Kwok, J.W.Y. Lam, B.Z. Tang, A highly fluorescent AIE-active theranostic agent with anti-tumor activity to specific cancer cells, *Nanoscale* 8 (25) (2016) 12520–12523.
- [6] S. Malik, R.M. Cusidó, M.H. Mirjalili, E. Moyano, J. Palazón, M. Bonfill, Production of the anticancer drug taxol in *Taxus baccata* suspension cultures: a review, *Process Biochem.* 46 (1) (2011) 23–34.
- [7] Y. Tu, The discovery of artemisinin (qinghaosu) and gifts from Chinese medicine, *Nat. Med.* 17 (10) (2011) 1217–1220.
- [8] D.A. Drew, Y. Cao, A.T. Chan, Aspirin and colorectal cancer: the promise of precision chemoprevention, *Nat. Rev. Cancer* 16 (3) (2016) 173–186.
- [9] Y. Gu, Z. Zhao, H. Su, P. Zhang, J. Liu, G. Niu, S. Li, Z. Wang, R.T.K. Kwok, X.-L. Ni, J. Sun, A. Qin, Jacky W.Y. Lam, B.Z. Tang, Exploration of biocompatible AIEgens from natural resources, *Chem. Sci.* 9 (31) (2018) 6497–6502.
- [10] M. Liong, J. Lu, M. Kovichich, T. Xia, S.G. Ruehm, A.E. Nel, F. Tamanoi, J.I. Zink, Multifunctional inorganic nanoparticles for imaging, targeting, and drug delivery, *ACS Nano* 2 (5) (2008) 889–896.
- [11] C. Chen, J. Geng, F. Pu, X. Yang, J. Ren, X. Qu, Polyvalent nucleic acid/mesoporous silica nanoparticle conjugates: dual stimuli-responsive vehicles for intracellular drug delivery, *Angew. Chem. Int. Ed.* 50 (4) (2011) 882–886.
- [12] A. Abhinav, K.T. Pushpendra, T. Shalini, K.J. Narendra, Fluorescence imaging: applications in drug delivery research, *curr. Drug Targets* 9 (10) (2008) 895–898.
- [13] A.-M. Pena, X. Chen, I.J. Pence, T. Bornschlöggl, S. Jeong, S. Grégoire, G.S. Luengo, P. Hallegot, P. Obeidy, A. Feizpour, K.F. Chan, C.L. Evans, Imaging and quantifying drug delivery in skin – Part 2: fluorescence and vibrational spectroscopic imaging methods, *Adv. Drug Deliv. Rev.* 153 (2020) 147–168.
- [14] C. Li, T. Dong, Q. Li, X. Lei, Probing the anticancer mechanism of (–)-Ainslatriamer A through diverted total synthesis and bioorthogonal ligation, *Angew. Chem. Int. Ed.* 53 (45) (2014) 12111–12115.
- [15] X. Xue, Y. Zhao, L. Dai, X. Zhang, X. Hao, C. Zhang, S. Huo, J. Liu, C. Liu, A. Kumar, W.-Q. Chen, G. Zou, X.-J. Liang, Spatiotemporal drug release visualized through a drug delivery system with tunable aggregation-induced emission, *Adv. Mater.* 26 (5) (2014) 712–717.
- [16] J. Mei, N.L.C. Leung, R.T.K. Kwok, J.W.Y. Lam, B.Z. Tang, Aggregation-induced emission: together we shine, united we soar, *Chem. Rev.* 115 (21) (2015) 11718–11940.
- [17] J. Yang, M. Fang, Z. Li, Organic luminescent materials: the concentration on aggregates from aggregation-induced emission, *Aggregate* 1 (1) (2020) 6–18.
- [18] D. Ding, K. Li, B. Liu, B.Z. Tang, Bioprobes based on AIE fluorogens, *Acc. Chem. Res.* 46 (11) (2013) 2441–2453.
- [19] L. Sun, J. Ouyang, Y. Ma, Z. Zeng, C. Zeng, F. Zeng, S. Wu, An activatable probe with aggregation-induced emission for detecting and imaging herbal medicine induced liver injury with optoacoustic imaging and NIR-II fluorescence imaging, *Adv. Healthc. Mater.* 10 (24) (2021), 2100867.
- [20] T. Zhou, R. Hu, L. Wang, Y. Qiu, G. Zhang, Q. Deng, H. Zhang, P. Yin, B. Situ, C. Zhan, A. Qin, B.Z. Tang, An AIE-active conjugated polymer with high ROS-generation ability and biocompatibility for efficient photodynamic therapy of bacterial infections, *Angew. Chem. Int. Ed.* 59 (25) (2020) 9952–9956.
- [21] R. Qu, X. Zhen, X. Jiang, Emerging designs of aggregation-induced emission agents for enhanced phototherapy applications, *CCS Chem.* 4 (2022) 401–419.

- [22] Y. Li, Z. Zhao, J. Zhang, R.T.K. Kwok, S. Xie, R. Tang, Y. Jia, J. Yang, L. Wang, J.W. Y. Lam, W. Zheng, X. Jiang, B.Z. Tang, A bifunctional aggregation-induced emission luminogen for monitoring and killing of multidrug-resistant bacteria, *Adv. Funct. Mater.* 28 (42) (2018), 1804632.
- [23] X. Ge, M. Gao, B. Situ, W. Feng, B. He, X. He, S. Li, Z. Ou, Y. Zhong, Y. Lin, X. Ye, X. Hu, B.Z. Tang, L. Zheng, One-step, rapid fluorescence sensing of fungal viability based on a bioprobe with aggregation-induced emission characteristics, *Mater. Chem. Front.* 4 (3) (2020) 957–964.
- [24] Y.L. Balachandran, X. Jiang, Aggregation-induced fluorogens in bio-detection, tumor imaging, and therapy: a review, *ACS Chem.* 4 (2022) 420–436.
- [25] B. Wang, H. Wu, R. Hu, X. Liu, Z. Liu, Z. Wang, A. Qin, B.Z. Tang, Cationic tricyclic AIEgens for concomitant bacterial discrimination and inhibition, *Adv. Healthc. Mater.* 10 (12) (2021), 2100136.
- [26] D. Wang, M.M.S. Lee, G. Shan, R.T.K. Kwok, J.W.Y. Lam, H. Su, Y. Cai, B.Z. Tang, Highly efficient photosensitizers with far-red/near-infrared aggregation-induced emission for in vitro and in vivo cancer theranostics, *Adv. Mater.* 30 (39) (2018), 1802105.
- [27] M. Kang, Z. Zhang, N. Song, M. Li, P. Sun, X. Chen, D. Wang, B.Z. Tang, Aggregation-enhanced theranostics: AIE sparkles in biomedical field, *Aggregate* 1 (1) (2020) 80–106.
- [28] D. Guo, L. Li, X. Zhu, M. Heeny, J. Li, L. Dong, Q. Yu, Z. Gan, X. Gu, L. Tan, Naphthalene diimide based near-infrared luminogens with aggregation-induced emission characteristics for biological imaging and high mobility ambipolar transistors, *Sci. China Chem.* 63 (9) (2020) 1198–1207.
- [29] C. Zhu, R.T.K. Kwok, J.W.Y. Lam, B.Z. Tang, Aggregation-induced emission: a trailblazing journey to the field of biomedicine, *ACS Appl. Bio Mater.* 1 (6) (2018) 1768–1786.
- [30] W. Zeng, Y. Xu, W. Yang, K. Liu, K. Bian, B. Zhang, An ultrasound-excitabile Aggregation-induced emission dye for enhanced sonodynamic therapy of tumors, *Adv. Healthc. Mater.* 9 (17) (2020), 2000560.
- [31] J. Dai, Y. Li, Z. Long, R. Jiang, Z. Zhuang, Z. Wang, Z. Zhao, X. Lou, F. Xia, B. Z. Tang, Efficient near-infrared photosensitizer with aggregation-induced emission for imaging-guided photodynamic therapy in multiple xenograft tumor models, *ACS Nano* 14 (1) (2020) 854–866.
- [32] G. Feng, W. Qin, Q. Hu, B.Z. Tang, B. Liu, Cellular and mitochondrial dual-targeted organic dots with aggregation-induced emission characteristics for image-guided photodynamic therapy, *Adv. Healthc. Mater.* 4 (17) (2015) 2667–2676.
- [33] N.K. Pandey, W. Xiong, L. Wang, W. Chen, B. Bui, J. Yang, E. Amador, M. Chen, C. Xing, A.A. Athavale, Y. Hao, W. Feizi, L. Lumata, Aggregation-induced emission luminogens for highly effective microwave dynamic therapy, *Bioact. Mater.* 7 (2022) 112–125.
- [34] X. Feng, B. Tong, J. Shi, C. Zhao, Z. Cai, Y. Dong, Recent progress of aggregation-induced emission luminogens (AIEgens) for bacterial detection and theranostics, *Mater. Chem. Front.* 5 (3) (2021) 1164–1184.
- [35] H.-F. Su, Q.-C. Peng, Y.U. Liu, T. Xie, P.-P. Liu, Y.-C. Cai, W. Wen, Y.-H. Yu, K. Li, S.-Q. Zang, A near-infrared AIE probe and its applications with specific in vitro and in vivo two-photon imaging of lipid droplets, *Biomaterials* 288 (2022), 121691.
- [36] H. Su, Z. Deng, Y. Liu, Y. Zhao, H. Liu, Z. Zhao, B.Z. Tang, A brightly red emissive AIEgen and its antibody conjugated nanoparticles for cancer cell targeting imaging, *Mater. Chem. Front.* 6 (10) (2022) 1317–1323.
- [37] J. Mei, Y. Hong, J.W.Y. Lam, A. Qin, Y. Tang, B.Z. Tang, Aggregation-induced emission: the whole is more brilliant than the parts, *Adv. Mater.* 26 (31) (2014) 5429–5479.
- [38] S. Basavojju, D. Boström, S.P. Velaga, Pharmaceutical cocrystal and salts of norfloxacin, *Cryst. Growth Des.* 6 (12) (2006) 2699–2708.
- [39] J.T.J. Freitas, C.C. de Melo, O.M.M.S. Viana, F.F. Ferreira, A.C. Doriguetto, Crystal structure of levofloxacin anhydrides: a high-temperature powder X-ray diffraction study versus crystal structure prediction, *Cryst. Growth Des.* 18 (6) (2018) 3558–3568.
- [40] J.-J. Qian, J.-M. Gu, J. Shen, X.-R. Hu, S.-X. Wu, Moxifloxacinium chloride monohydrate, *Acta Crystallogr. E* 67 (10) (2011) o2773–o2774.
- [41] Y.-Q. Hu, S. Zhang, Z. Xu, Z.-S. Lv, M.-L. Liu, L.-S. Feng, 4-Quinolone hybrids and their antibacterial activities, *Eur. J. Med. Chem.* 141 (2017) 335–345.
- [42] A.N. Fallica, C. Barbaraci, E. Amata, L. Pasquiniucci, R. Turnaturi, M. Dichiaro, S. Intagliata, M.B. Gariboldi, E. Marras, V.T. Orlandi, C. Ferroni, C. Martini, A. Rescifina, D. Gentile, G. Varchi, A. Marrazzo, Nitric oxide photo-donor hybrids of ciprofloxacin and norfloxacin: a shift in activity from antimicrobial to anticancer agents, *J. Med. Chem.* 64 (15) (2021) 11597–11613.
- [43] M. Kang, C. Zhou, S. Wu, B. Yu, Z. Zhang, N. Song, M.M.S. Lee, W. Xu, F.-J. Xu, D. Wang, L. Wang, B.Z. Tang, Evaluation of structure–function relationships of aggregation-induced emission luminogens for simultaneous dual applications of specific discrimination and efficient photodynamic killing of gram-positive bacteria, *J. Am. Chem. Soc.* 141 (42) (2019) 16781–16789.
- [44] C. Zhou, W. Xu, P. Zhang, M. Jiang, Y. Chen, R.T.K. Kwok, M.M.S. Lee, G. Shan, R. Qi, X. Zhou, J.W.Y. Lam, S. Wang, B.Z. Tang, Engineering sensor arrays using aggregation-induced emission luminogens for pathogen identification, *Adv. Funct. Mater.* 29 (4) (2019), 1805986.
- [45] J. Zielonka, J. Joseph, A. Sikora, M. Hardy, O. Ouari, J. Vasquez-Vivar, G. Cheng, M. Lopez, B. Kalyanaraman, Mitochondria-targeted triphenylphosphonium-based compounds: syntheses, mechanisms of action, and therapeutic and diagnostic applications, *Chem. Rev.* 117 (15) (2017) 10043–10120.
- [46] H. Huang, L. Yang, P. Zhang, K. Qiu, J. Huang, Y. Chen, J. Diao, J. Liu, L. Ji, J. Long, H. Chao, Real-time tracking mitochondrial dynamic remodeling with two-photon phosphorescent iridium (III) complexes, *Biomaterials* 83 (2016) 321–331.
- [47] B.N.G. Giepmans, S.R. Adams, M.H. Ellisman, R.Y. Tsien, The fluorescent toolbox for assessing protein location and function, *Science* 312 (5771) (2006) 217–224.
- [48] A.L. Antaris, H. Chen, K. Cheng, Y. Sun, G. Hong, C. Qu, S. Diao, Z. Deng, X. Hu, B. Zhang, X. Zhang, O.K. Yaghi, Z.R. Alamparambil, X. Hong, Z. Cheng, H. Dai, A small-molecule dye for NIR-II imaging, *Nat. Mater.* 15 (2) (2016) 235–242.
- [49] H.-Y. Kwon, X. Liu, E.G. Choi, J.Y. Lee, S.-Y. Choi, J.-Y. Kim, L. Wang, S.-J. Park, B. Kim, Y.-A. Lee, J.-J. Kim, N.Y. Kang, Y.-T. Chang, Development of a universal fluorescent probe for gram-positive bacteria, *Angew. Chem. Int. Ed.* 58 (25) (2019) 8426–8431.
- [50] A. Duarte, A. Chworos, S.F. Flagan, G. Hanrahan, G.C. Bazan, Identification of bacteria by conjugated oligoelectrolyte/single-stranded DNA electrostatic complexes, *J. Am. Chem. Soc.* 132 (36) (2010) 12562–12564.
- [51] C. Zhu, L. Liu, Q. Yang, F. Lv, S. Wang, Water-soluble conjugated polymers for imaging, diagnosis, and therapy, *Chem. Rev.* 112 (8) (2012) 4687–4735.
- [52] H. Yuan, Z. Liu, L. Liu, F. Lv, Y. Wang, S. Wang, Cationic conjugated polymers for discrimination of microbial pathogens, *Adv. Mater.* 26 (25) (2014) 4333–4338.
- [53] H. Pei, J. Li, M. Lv, J. Wang, J. Gao, J. Lu, Y. Li, Q. Huang, J. Hu, C. Fan, A graphene-based sensor array for high-precision and adaptive target identification with ensemble aptamers, *J. Am. Chem. Soc.* 134 (33) (2012) 13843–13849.
- [54] W. Chen, Q. Li, W. Zheng, F. Hu, G. Zhang, Z. Wang, D. Zhang, X. Jiang, Identification of bacteria in water by a fluorescent array, *Angew. Chem. Int. Ed.* 53 (50) (2014) 13734–13739.
- [55] J. Gao, L. Li, P.-L. Ho, G.C. Mak, H. Gu, B. Xu, Combining fluorescent probes and biofunctional magnetic nanoparticles for rapid detection of bacteria in human blood, *Adv. Mater.* 18 (23) (2006) 3145–3148.
- [56] H. Bai, W. He, J.H.C. Chau, Z. Zheng, R.T.K. Kwok, J.W.Y. Lam, B.Z. Tang, AIEgens for microbial detection and antimicrobial therapy, *Biomaterials* 268 (2021), 120598.
- [57] D.C. Hooper, Mechanisms of fluoroquinolone resistance, *Drug Resist. Updates* 2 (1) (1999) 38–55.
- [58] M.A. Kohanski, D.J. Dwyer, B. Hayete, C.A. Lawrence, J.J. Collins, A common mechanism of cellular death induced by bactericidal antibiotics, *Cell* 130 (5) (2007) 797–810.
- [59] Z. Zhang, W. Xu, M. Kang, H. Wen, H. Guo, P. Zhang, L. Xi, K. Li, L. Wang, D. Wang, B.Z. Tang, An all-round athlete on the track of phototheranostics: subtly regulating the balance between radiative and nonradiative decays for multimodal imaging-guided synergistic therapy, *Adv. Mater.* 32 (36) (2020), 2003210.